Article:

Onset of interchange instability in a coupled core–SOL plasma

Fryderyk Wilczynski,[1, a)] David W. Hughes,[1] Wayne Arter,[2] and Fulvio Militello[2]

[1)] *School of Mathematics, University of Leeds, Leeds LS2 9JT, United Kingdom*

[2)] *CCFE, Culham Science Centre, Abingdon OX14 3DB, United Kingdom*

The dynamics at the edge of fusion confinement devices is driven by interchange instabilities and involves the motion of plasma across two regions — the 'core region' and the scrape-off layer (SOL), distinguished by whether field lines are, respectively, closed or connected to the wall. Motivated by this phenomenon, we present an extensive linear stability analysis of a two-layer plasma model encompassing the coupled interactions between the region with closed field lines and the SOL. We focus on the effect of varying the particle diffusivity and ion viscosity, revealing the significant variation in the spatial structure of the critical modes. In addition, we have investigated the dependence of the stability threshold on the ratio of the width of the region with closed field lines to that of the SOL; this dependence is strong when the ratio is sufficiently small, but becomes insignificant once the ratio is of order unity.

I. INTRODUCTION

The dynamics at the edge of magnetic confinement fusion devices involves the turbulent transport of plasma from the well-confined core, through the scrape-off layer (SOL), towards the material surfaces. It has been universally observed that turbulence in the SOL is characterized by intermittent ejection of coherent filamentary structures[1,2]. These filaments dominate the particle transport and enhance the plasma interaction with the surrounding material boundaries. This is problematic on two fronts: plasma-wall interactions can potentially damage plasma-facing components and shorten the life-time of the device; furthermore, energy losses associated with the ejection of filaments inhibit fusion reactions in the confinement region, thus diminishing the performance of the tokamak. As fusion power increases, so does the erosive potential of filaments; understanding the dynamics of filaments therefore plays a vital role in the successful operation of future, more powerful fusion reactors, such as ITER and DEMO.

It is widely recognized that turbulence in the SOL is driven by a combination of interchange dynamics, due to pressure gradients and magnetic field curvature, and drift-Alfvén waves. Since drift-Alfvén waves are strongly damped on open field lines, turbulent motions in the SOL are dominated by interchange dynamics, supplemented by parallel losses and sheath dissipation at the plasma-solid interface[3]. Over the years, numerous interchange models, of various complexity, have been developed, which successfully capture several experimentally measured features of the midplane SOL plasma. Initial models focused solely on the dynamics in the SOL region[4–8], in which turbulence was driven by the inclusion of a local source term. Subsequently, motivated by the concept that turbulence originates in the core, the simple SOL models have been extended to consider a configuration composed of two regions, one representing the
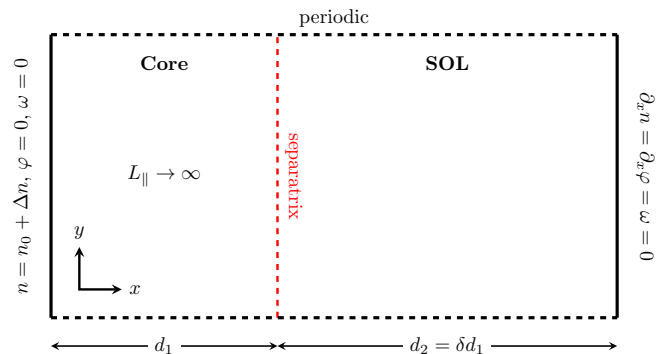
a)Electronic mail: amtfw@leeds.ac.uk

FIG. 1: Schematic of the two-region configuration.

core and the other the SOL, as sketched in Fig. 1. The two regions are separated by a magnetic separatrix and exhibit distinct dynamics parallel to the magnetic field. In the 'core', corresponding to flux surfaces interior to the Last Closed Flux Surface (LCFS), the magnetic field lines close back upon themselves and do not come in contact with material surfaces. By contrast, in the SOL, the magnetic field lines are open, in the sense that they penetrate a solid surface. Since every field line in the SOL is connected to a material surface, the SOL plasma is always subject to parallel losses of particles and energy.

One of the most notable early models in the edge-SOL drift fluid modelling campaign was ESEL[9], a two-dimensional interchange model consisting of evolution equations for density, vorticity, and electron temperature. Computations using ESEL successfully reproduce intermittent ejection of coherent plasma blobs from the core region, and their subsequent propagation into the SOL. Furthermore, ESEL has been successful in capturing properties of SOL turbulence, with reports of significant points of agreement with tokamak experiments on TCV[10,11], JET[12], EAST[13], and MAST[14,15]. The agreement between the simulation results and experimental data was established based on the comparison of the statistics of experimental measurements using Langmuir probes with the statistics of single-point recordings from

Machine	D_n	μ	Reference
TCV	10^{-2}	10^{-2}	Garcia $et\ al.$[16,17]
TCV	4.5×10^{-3}	2.5×10^{-2}	Garcia $et\ al.$[10]
TCV	4.5×10^{-3}	8.5×10^{-3}	Fundamenski $et\ al.$[12]
JET	2.9×10^{-4}	3.1×10^{-3}	Fundamenski $et\ al.$[12]
TCV	4.7×10^{-3}	—	Militello $et\ al.$[14]
MAST	1.95×10^{-3}	—	Militello $et\ al.$[14]
MAST	1.21×10^{-2}	1.13×10^{-1}	Militello $et\ al.$[15]
EAST	1.8×10^{-3}	3.5×10^{-2}	Yan $et\ al.$[13]

TABLE I: Example values of ion viscosity μ and particle diffusivity D_n used in ESEL simulations, where the values have been normalized with respect to Bohm diffusion (see Sec. II B for details); the missing data values are not explicitly reported.

synthetic probes within the simulation domain. Significant agreement between simulation and experimental data has also been found in terms of observations of radial profiles of time-averaged particle density and radial particle flux, as well as probability distribution functions of their fluctuations.

Although simulations of the nonlinear regime provide a valuable insight into the dynamics of the plasma, they cannot tell the whole story. Each numerical simulation necessarily studies one particular set-up (e.g. parameter values and geometrical configuration); such computations are though inherently expensive, and can thus provide only fragmentary information. A complementary approach is provided by a detailed linear stability analysis, which, surprisingly, has not been performed for this problem. Such an analysis allows a comprehensive exploration of the nature of the onset of instability and its dependence on the various parameter values and on the geometrical set-up.

Even the simplest interchange models admit a substantial number of physical parameters, such as curvature drive, perpendicular diffusion coefficients, and parallel dissipation rates. These parameters differ between each study, depending on the machine and the particular discharge modelled. Differences between machine parameters (such as magnetic field, radius of curvature, safety factor, parallel connection length) and plasma conditions between different discharges (such as plasma density, electron and ion temperature) lead to a significant variability in terms of the values of physical model parameters used in the simulations. For example, Table I highlights the variability in the values of particle diffusivity and ion viscosity in ESEL simulations. With the variability in terms of the physical parameters used, it is clearly of interest to determine if there is the possibility of different regimes of behavior.

Another source of variability comes from the differences in the two geometrical parameters of the numerical domain. One of these is the ratio of the width of the core region to that of the SOL in the model ($d_1 : d_2$ in Fig. 1). The physical processes associated with these regions are very different: the core region is responsible for turbulence production, whereas the SOL is responsible for dissipation to the sheath. It is therefore reasonable to expect that this ratio of widths could play a role in terms of the onset of instability and subsequent nonlinear evolution of the system. The other relevant geometrical parameter is the aspect ratio between the radial and the poloidal extent of the numerical domain. Analytically, one can assume periodicity in the poloidal direction of arbitrary wavelength; computationally, however, the wavelengths are constrained by the finite poloidal extent of the domain. Knowledge of the critical wavelength at the onset of instability can therefore guide the choice of an appropriate aspect ratio, thereby avoiding the possibility of artificially constraining the intensity of turbulence by restricting the system to slower growing modes.

A deeper understanding of the onset of the underlying interchange instabilities could be of great benefit in the study of edge turbulence and SOL filament generation. For example, without knowledge of the stability threshold, it is difficult to judge how supercritical (i.e. how far into the nonlinear regime) are the simulations performed. Here, we perform a linear stability analysis of a simple two-dimensional fluid model for interchange plasma dynamics in a configuration that encompasses both the core and the SOL regions. Given the distinct properties of the two regions, the most elegant and efficient means of tackling the problem is by a two-layer approach with matching conditions at the separatrix. We characterize the onset of instability and perform an extensive analysis to describe how the behavior of the system varies as a function of plasma parameters and geometrical configuration. The work presented here may therefore be viewed as an extension of our two earlier studies[18,19]. In the former, we restricted our attention solely to the dynamics in the SOL, as well as exploring the analogy between the interchange instability in the plasma edge and that of Rayleigh-Bénard convection. In the latter, we considered the conceptually simpler two-layer problem of the convective instability of two superposed miscible neutral fluids.

The remainder of the paper is structured as follows. In Section II we introduce the governing equations, together with the conditions to be satisfied at the boundaries and at the separatrix. Section III contains the formulation of the marginal stability problem, and the results are analysed in Section IV. A concluding discussion is contained in Section V.

II. MATHEMATICAL FORMULATION

A. Governing equations

The starting point of our analysis is the electrostatic drift fluid model of Easy $et\ al.$[20,21]. The model assumes cold ions, isothermal electrons, and the Boussinesq approximation. The geometry is simplified to a local slab with a uniform magnetic field $\boldsymbol{B} = B\hat{\boldsymbol{z}}$; the effects of

magnetic curvature and inhomogeneity of $\boldsymbol{B}$ are then represented through additional effective gravity terms acting in the radial direction. Coordinates x and y represent the effective radial and poloidal directions, respectively. The evolution of plasma potential φ and electron density n_e are determined by the plasma vorticity and density equations:

$$\frac{m_i n_e}{B} \left(\frac{\partial}{\partial t} + \boldsymbol{v}_E \cdot \nabla + v_{\|i} \nabla_\| \right) \omega = \nabla_\| j_\| - \frac{eg}{\Omega_i} \frac{\partial n_e}{\partial y} + \frac{n_e m_i \nu_i}{B} \nabla_\perp^2 \omega, \tag{1}$$

$$\frac{\partial n_e}{\partial t} + \boldsymbol{v}_E \cdot \nabla n_e + \nabla_\| \left(v_{\|e} n_e \right) = \frac{g n_e}{B c_s^2} \frac{\partial \varphi}{\partial y} - \frac{g}{\Omega_i} \frac{\partial n_e}{\partial y} + D\nabla_\perp^2 n_e + s_n. \tag{2}$$

Here, $\omega = \nabla_\perp^2 \varphi / B$ is the plasma vorticity, $\boldsymbol{v}_E = B^{-1}(\hat{\boldsymbol{b}} \times \nabla\varphi)$ is the $\boldsymbol{E} \times \boldsymbol{B}$ drift velocity, and $j_\| = en\left(v_{\|i} - v_{\|e} \right)$ is the parallel current density, where $v_{\|i}$ $(v_{\|e})$ is the parallel ion (electron) velocity; s_n is a particle source, ν_i represents the effective cross field kinematic viscosity of ions, D is the collisional diffusion coefficient, e is the elementary unit charge, m_i is the ion mass. Parameter $g = 2c_s^2/R_c$ represents the effective gravitational acceleration that captures the influence of magnetic gradients and curvature; $c_s = \sqrt{T_e/m_i}$ is the sound speed, T_e is the electron temperature in Joules, and R_c is the radius of curvature (typically the major radius of the machine). The ion gyrofrequency $\Omega_i = eB/m_i$ is related to the sound speed through the gyroradius $\rho_s = c_s/\Omega_i$. Equation (1) is a statement of the current conservation law $\nabla \cdot \boldsymbol{J} = 0$, with individual terms, from the left hand side, representing divergences of ion polarization current density, parallel current density, electron diamagnetic current density and perpendicular current density due to ion viscosity.

As presented, equations (1), (2) are incomplete. To form a self-consistent system we need to provide descriptions for the parallel ion and electron velocities. This can be achieved by constructing additional evolution equations for parallel momenta, although such an approach requires a three-dimensional treatment. Alternatively, the dynamics of plasma parallel to the magnetic field can be modelled by implementation of a suitable closure for the current along the field lines.

Here we pursue the latter option and restrict our attention to the dynamics perpendicular to the magnetic field. We consider an outboard midplane region of the plasma edge that encompasses both a representation of the core region and the scrape-off layer, as depicted in Fig. 1. In the SOL the field lines end with a Debye sheath at a material surface, which provides a sink for plasma particles. A simplified description of the effect of sheath currents on the collective plasma dynamics can be obtained by averaging the model equations along the field lines and invoking the sheath dissipation closure. This closure scheme

assumes negligible gradients of density and potential in the parallel direction and also that parallel current is regulated by the sheath boundary conditions[22,23],

$$v_{\|i}(z = \pm l_\|) = \pm c_s, \tag{3}$$

$$v_{\|e}(z = \pm l_\|) = \pm c_s \exp\left(-\frac{e}{T_e}\varphi \right), \tag{4}$$

where $l_\|$ is the parallel SOL connection length — typically the mid-plane to target distance.

In order to confine the dynamics to the plane perpendicular to the imposed magnetic field, we require an average over the parallel direction, defined by

$$\langle \cdot \rangle = \frac{1}{2l_\|} \int_{-l_\|}^{+l_\|} \mathrm{d}z. \tag{5}$$

In the vorticity equation (1), the average of the divergence of the parallel current gives

$$\langle \nabla_\| j_\| \rangle = \frac{ec_s n_e}{l_\|} \left(1 - \exp\left(-\frac{e}{T_e}\varphi \right) \right), \tag{6}$$

while the term $v_{\|i}\nabla_\|\omega$ vanishes on the assumption that ω does not vary in the parallel direction. In the continuity equation (2), the averaged parallel particle flux becomes

$$\langle \nabla_\| \left(v_{\|e} n_e \right) \rangle = \frac{c_s n_e}{l_\|} \exp\left(-\frac{e}{T_e}\varphi \right). \tag{7}$$

Here, n_0 is the constant reference density maintained by the source term[20,24], i.e.,

$$\langle s_n \rangle = \frac{c_s}{l_\|} n_0. \tag{8}$$

In the core region, the field lines are closed, and hence the parallel direction can be considered periodic. Thus, on integration along the field lines, all parallel terms including the source term vanish. On adopting $x = 0$ as the position of the separatrix, the two-dimensional governing equations become:

$$\frac{\partial \omega}{\partial t} + \boldsymbol{v}_E \cdot \nabla \omega = -\frac{g}{n_e}\frac{\partial n_e}{\partial y} + \nu_i \nabla^2 \omega + H(x)\Lambda_\omega, \tag{9}$$

$$\frac{\partial n_e}{\partial t} + \boldsymbol{v}_E \cdot \nabla n_e = \frac{g n_e}{B c_s^2}\frac{\partial \varphi}{\partial y} - \frac{g}{\Omega_i}\frac{\partial n_e}{\partial y} + D\nabla^2 n_e + H(x)\Lambda_n, \tag{10}$$

where

$$\Lambda_\omega = \frac{1}{l_\|} c_s \Omega_i \left(\frac{e}{T_e}\varphi \right), \tag{11}$$

$$\Lambda_n = \frac{c_s}{l_\|} n_0 - \frac{c_s}{l_\|} n_e \left(1 - \frac{e}{T_e}\varphi \right), \tag{12}$$

are the linearized versions of the parallel loss terms in the SOL due to sheath dissipation. Here, $H(x)$ is the Heaviside function, and n_0 is a constant reference SOL density.

An alternative prescription for the transition from closed to open field line regions, which is commonly used in the literature (e.g. Madsen *et al.* [25]), is a smoothly varying tanh function; however, such an approach introduces an additional parameter describing the narrow transition width. Equations (9) and (10) are to be solved subject to the following radial boundary conditions [10,14]:

$$\varphi = \omega = 0, \quad n = n_0 + \Delta n \quad \text{at} \quad x = -d_1, \quad (13)$$

$$\frac{\partial \varphi}{\partial x} = \omega = \frac{\partial n}{\partial x} = 0 \quad \text{at} \quad x = d_2. \quad (14)$$

The poloidal direction is considered to be periodic.

B. Normalization

Conventionally, in edge plasma literature the governing equations appear in Bohm-normalized form obtained by scaling length with ρ_s, time with Ω_i^{-1}, density with n_0, potential with T_e/e. Equations (9), (10), scaled according to Bohm normalization, become

$$\frac{d\omega}{dt} = -\frac{\hat{g}}{n}\frac{\partial n}{\partial y} + \mu \nabla^2 \omega + H(x)\frac{\varphi}{L_\parallel}, \quad (15)$$

$$\frac{dn}{dt} = n\hat{g}\frac{\partial \varphi}{\partial y} - \hat{g}\frac{\partial n}{\partial y} + D_n \nabla^2 n + H(x)\left(\frac{n\varphi}{L_\parallel} - \frac{n-1}{L_\parallel}\right), \quad (16)$$

where

$$\hat{g} = \frac{g}{\rho_s \Omega_i^2} = \frac{2\rho_s}{R_c}, \qquad L_\parallel = \frac{l_\parallel}{\rho_s},$$

$$D_n = \frac{D}{D_{\text{Bohm}}}, \qquad \mu = \frac{\nu_i}{D_{\text{Bohm}}}, \quad (17)$$

are the normalized effective gravitational acceleration, parallel connection length, particle diffusion and viscosity, respectively, and $D_{\text{Bohm}} = \rho_s^2 \Omega_i$ is Bohm diffusion.

Formally, equations (15), (16) constitute a two-region version of the model studied in Easy *et al.* [20] (their equations (8), (7)). The model considered here is different from ESEL in terms of the following aspects. First, the ESEL model includes evolution of electron temperature, and, in this respect, it could be considered more complicated. Here, we consider the idealized isothermal limit, whereby the electron temperature is assumed constant. Second, the ESEL model employs the so-called thin layer approximation [25]. This approximation neglects particle density variations in the polarization flux entering the vorticity equation and hence assumes a constant inertia of all fluid parcels, irrespective of the local particle density. As a consequence, in the ESEL model, the density variation $1/n$ in front of the first term on the vorticity equation (15) is neglected (see for example equation (20c) in Garcia *et al.* [16]). Third, in ESEL the parallel losses of particle density and vorticity in the region of open field lines are modelled using the vorticity advection closure.

In our model, parametrization of parallel losses is based on the sheath dissipation closure.

The Bohm-normalized equations (15), (16) evolve on the time scale given by the ion gyrofrequency, Ω_i^{-1}. On the other hand, according to the underlying assumptions behind drift-ordered models, the system should evolve on a much slower time scale given by the dynamical frequency (the dynamical frequency is much smaller than the gyrofrequency [26]). Furthermore, in light of the analysis in Wilczynski *et al.* [18], we expect the length scale of the convective cells to be comparable with the radial extent of the domain, and thus much larger than the gyroradius ρ_s. Therefore, we shall proceed with the alternative nondimensionalization based on the diffusion timescale; on scaling time with d_1^2/D, length with d_1, potential with BD, density with n_0, equations (9), (10) become

$$\frac{d\omega}{dt} = -Ra^* Pr \frac{1}{n}\frac{\partial n}{\partial y} + Pr\nabla^2 \omega + H(x)\frac{L_\perp^2 \Omega}{L_\parallel}\varphi, \quad (18)$$

$$\frac{dn}{dt} = \zeta n \frac{\partial \varphi}{\partial y} - \frac{Ra^* Pr}{\Omega}\frac{\partial n}{\partial y} + \nabla^2 n + H(x)\left(\frac{L_\perp^2}{L_\parallel}n\varphi - \frac{\Omega}{L_\parallel}(n-1)\right). \quad (19)$$

The dimensionless parameters are

$$Ra^* = \frac{gd_1^3}{D\nu_i}, \qquad Pr = \frac{\nu_i}{D}, \qquad \Omega = \frac{\Omega_i d_1^2}{D},$$

$$L_\parallel = \frac{l_\parallel}{\rho_s}, \qquad L_\perp = \frac{d_1}{\rho_s}, \qquad \zeta = \frac{2d_1}{R_c}. \quad (20)$$

The parameter Ra^* measures the ratio of the strength of the curvature-induced gravitational force to viscous forces. It is similar to the Rayleigh number associated with buoyancy-driven flow, although this analogy is not complete since Ra^* is missing a factor describing the density difference (or temperature difference in convection) across the layer. Pr can be thought of as equivalent to the Prandtl number in the convection problem, but instead of describing the ratio of fluid viscosity to thermal diffusivity, here it represents the ratio of ion viscosity to particle diffusivity. Ω is the gyrofrequency divided by the frequency given by the diffusion time scale. $L_\parallel$ is the normalized measure of parallel connection length, and $L_\perp$ is the normalized measure of the width of the layer. Finally, the parameter ζ is representative of the effect of compressibility of the $\boldsymbol{E} \times \boldsymbol{B}$ drift. These are related to the traditional Bohm plasma parameters (17) as follows:

$$Ra^* = \frac{\hat{g}L_x^3}{D_n \mu}, \qquad Pr = \frac{\mu}{D_n}, \qquad \Omega = \frac{L_x^2}{D_n},$$

$$\zeta = \hat{g}L_x, \qquad L_\perp = L_x, \quad (21)$$

where L_x is the Bohm-normalized radial length of the core region under consideration.

As outlined briefly in the Introduction, differences in plasma conditions between discharges lead to considerable variability in the values of the physical parameters. In particular, D_n and μ admit a wide range

of values, depending on the edge plasma density and temperature. Evaluating the diffusion coefficients using neoclassical expressions[12], assuming MAST machine parameters ($q = 7$, $B = 0.5$T, $R_c = 0.85$m[14]), with plasma density and electron temperature in the ranges $n_e \in [10^{18}, 10^{20}\,\text{m}^{-3}]$, $T_e \in [10, 100\,\text{eV}]$, yields values of D_n and μ that range between $10^{-4} - 10^{-1}$ and $10^{-3} - 1$ respectively. Variation in the possible values of $\hat{g}$, which is independent of plasma density, is modest in comparison.

Throughout our analysis, we therefore focus on the effect of varying D_n and μ, and fix $\hat{g} = 2.4 \times 10^{-3}$, $L_\perp = 50$ (implying that $\zeta = 0.12$), $L_\parallel = 5500$. Numerically, we explore values of D_n in the range $10^{-3} - 1$ and μ in the range $10^{-3} - 1$. At small values of D_n, the problem becomes numerically stiff, and thus exploring values of D_n below 10^{-3} is computationally prohibitive. Recall that varying D_n and μ affects Ra^*, Pr and Ω according to (21). Thus, variation of μ affects only the diffusion term in the vorticity equation (18) and no terms in the density equation (19), whereas variation of D_n affects all terms on the right hand side in the vorticity equation, as well as the second and the final term on the right hand side of the density equation.

III. LINEAR STABILITY ANALYSIS

A. Basic state

We consider a steady basic state with plasma at rest, and assume that the basic state plasma density varies as a function only of the radial coordinate. We describe the basic state by upper case variables; thus $\Phi_k = 0$ and $n_k = N_k(x)$. The basic state density distribution is given by

$$\frac{\mathrm{d}^2 N_1}{\mathrm{d}x^2} = 0, \qquad -1 \le x < 0, \qquad (22)$$

$$\frac{\mathrm{d}^2 N_2}{\mathrm{d}x^2} - \frac{\Omega}{L_\parallel} N_2 = -\frac{\Omega}{L_\parallel}, \qquad 0 < x \le \delta, \qquad (23)$$

where indices $k = 1, 2$ denote core and SOL regions respectively and $\delta = d_2/d_1$ denotes the dimensionless width of the SOL. Boundary conditions on density (cf. (13), (14)), and the continuity of density and density flux at the separatrix require that

$$N_1 = 1 + \Delta n \qquad \text{at} \qquad x = -1, \quad (24)$$

$$\frac{\mathrm{d}N_2}{\mathrm{d}x} = 0 \qquad \text{at} \qquad x = \delta, \quad (25)$$

$$N_1 = N_2, \qquad \frac{\mathrm{d}N_1}{\mathrm{d}x} = \frac{\mathrm{d}N_2}{\mathrm{d}x} \qquad \text{at} \qquad x = 0. \quad (26)$$

Solving (22), (23) subject to conditions (24)–(26) yields

$$N_1 = 1 + \Delta n \left(1 + A_1 \left(x + 1\right)\right), \qquad (27)$$

$$N_2 = 1 + \Delta n \left(A_2 \cosh(\alpha x) + B_2 \sinh(\alpha x)\right), \qquad (28)$$
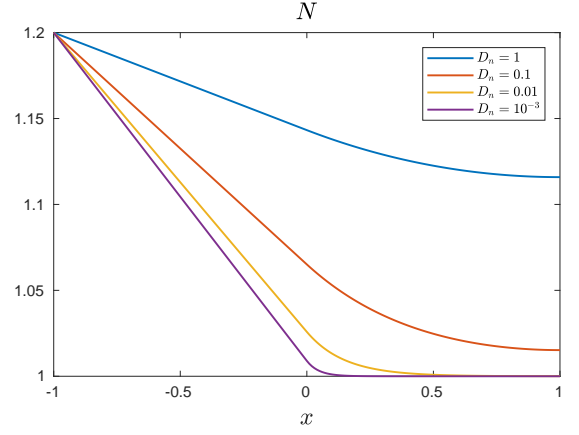

FIG. 2: Basic state profiles for varying values of D_n, with other parameters fixed: $\Delta n = 0.2$, $\delta = 1$, $L_\perp = 50$, $L_\parallel = 5500$.

where $\alpha = (\Omega/L_\parallel)^{1/2} = L_\perp/(D_n L_\parallel)^{1/2}$ and

$$A_1 = \frac{-\alpha \tanh(\alpha\delta)}{(1 + \alpha \tanh(\alpha\delta))}, \quad A_2 = \frac{1}{(1 + \alpha \tanh(\alpha\delta))},$$
$$B_2 = \frac{-\tanh(\alpha\delta)}{(1 + \alpha \tanh(\alpha\delta))}. \quad (29)$$

Figure 2 shows plots of the basic state density distribution for varying values of D_n. We note that the basic state depends explicitly on the value of the particle diffusivity D_n and parallel connection length $L_\parallel$. This indicates that the equilibrium density profile arises from the balance between perpendicular diffusion and parallel losses. In particular, when the diffusivity D_n is small (α is large), the SOL is loss dominated, and the density profile in the SOL approaches a uniform reference density (as $\alpha x \to \infty$, $N_2 \to 1$); this is illustrated in Fig. 2 for $D_n = 10^{-3}$. On the other hand, for sufficiently large D_n (small α), diffusion dominates over parallel losses and the equilibrium density in the SOL exceeds the constant reference value, as illustrated for the case of $D_n = 1$.

B. Linear perturbations equations

On introducing the change of variable $\theta = \log(n)$, the governing equations (19), (18) become

$$\frac{\mathrm{d}\omega}{\mathrm{d}t} = -Ra^* Pr \frac{\partial\theta}{\partial y} + Pr\nabla^2\omega + H(x)\frac{L_\perp^2 \Omega}{L_\parallel}\varphi, \qquad (30)$$

$$\frac{\mathrm{d}\theta}{\mathrm{d}t} = \zeta\frac{\partial\varphi}{\partial y} - \frac{Ra^* Pr}{\Omega}\frac{\partial\theta}{\partial y} + \nabla^2\theta + |\nabla\theta|^2$$
$$+ H(x)\left(\frac{L_\perp^2}{L_\parallel}\varphi - \frac{\Omega}{L_\parallel}\left(1 - \exp(-\theta)\right)\right). \qquad (31)$$

Note that the basic state equation (23) written in terms of $\Theta_2(x) = \log(N_2(x))$ becomes

$$\Theta_2'' + \Theta_2'^2 - \frac{\Omega}{L_\parallel}\left(1 - \exp(-\Theta_2)\right) = 0. \qquad (32)$$

We now consider small perturbations to this basic state, expressing the potential, vorticity and log-density in the perturbed state by φ_k, ω_k and $\Theta_k + \theta_k$ respectively. On substituting these expressions into equations (30) and (31) and retaining only the lowest order terms in the perturbations, the linearized forms of the equations of motion become

$$\frac{\partial \omega_1}{\partial t} = -Ra^* Pr \frac{\partial \theta_1}{\partial y} + Pr\nabla^2 \omega_1, \qquad (33)$$

$$\frac{\partial \theta_1}{\partial t} = (\Theta_1'(x) + \zeta)\frac{\partial \varphi_1}{\partial y} - \frac{Ra^* Pr}{\Omega}\frac{\partial \theta_1}{\partial y} + \nabla^2 \theta_1 + 2\Theta_1'(x)\frac{\partial \theta_1}{\partial x}, \qquad (34)$$

$$\frac{\partial \omega_2}{\partial t} = -Ra^* Pr \frac{\partial \theta_2}{\partial y} + Pr\nabla^2 \omega_2 + \frac{L_\perp^2 \Omega}{L_\parallel}\varphi_2, \qquad (35)$$

$$\frac{\partial \theta_2}{\partial t} = (\Theta_2'(x) + \zeta)\frac{\partial \varphi_2}{\partial y} - \frac{Ra^* Pr}{\Omega}\frac{\partial \theta_2}{\partial y} + \nabla^2 \theta_2$$
$$+ 2\Theta_2'(x)\frac{\partial \theta_2}{\partial x} - \frac{1}{N_2(x)}\frac{\Omega}{L_\parallel}\theta_2 + \frac{L_\perp^2}{L_\parallel}\varphi_2. \qquad (36)$$

The perturbation variables satisfy the following boundary conditions (cf. (13), (14)):

$$\varphi = \omega = \theta = 0 \qquad \text{at} \qquad x = -1, \qquad (37)$$
$$\partial_x \varphi = \omega = \partial_x \theta = 0 \qquad \text{at} \qquad x = \delta. \qquad (38)$$

Additionally, continuity of velocity, tangential and normal stress, density and density flux are satisfied at the separatrix:

$$\varphi_1 = \varphi_2, \qquad \frac{\partial \varphi_1}{\partial x} = \frac{\partial \varphi_2}{\partial x},$$
$$\frac{\partial^2 \varphi_1}{\partial x^2} - \frac{\partial^2 \varphi_1}{\partial y^2} = \frac{\partial^2 \varphi_2}{\partial x^2} - \frac{\partial^2 \varphi_2}{\partial y^2},$$
$$\frac{\partial}{\partial x}\left(\frac{\partial^2 \varphi_1}{\partial x^2} + 3\frac{\partial^2 \varphi_1}{\partial y^2}\right) = \frac{\partial}{\partial x}\left(\frac{\partial^2 \varphi_2}{\partial x^2} + 3\frac{\partial^2 \varphi_2}{\partial y^2}\right),$$
$$\theta_1 = \theta_2, \qquad \frac{\partial \theta_1}{\partial x} = \frac{\partial \theta_2}{\partial x} \qquad \text{at} \qquad x = 0. \qquad (39)$$

C. Marginal stability analysis

We seek normal mode solutions of the form

$$\varphi_k(x, y, t) = \hat{\varphi}_k(x)\exp\left(iky + \sigma t\right) + c.c., \qquad (40)$$
$$\theta_k(x, y, t) = \hat{\theta}_k(x)\exp\left(iky + \sigma t\right) + c.c., \qquad (41)$$

where k is the poloidal wavenumber and σ is the growth rate, which can, in general, be complex: $\sigma = s + i\gamma$;

$s, \gamma \in \mathbb{R}$. Substituting these expressions into equations (33)–(36) yields

$$\sigma\left(\mathcal{D}^2 - k^2\right)\hat{\varphi}_1 = -ikRa^* Pr\,\hat{\theta}_1 \\ + Pr\left(\mathcal{D}^4 - 2k^2\mathcal{D}^2 + k^4\right)\hat{\varphi}_1, \qquad (42)$$

$$\sigma\hat{\theta}_1 = ik\left(\Theta_1'(x) + \zeta\right)\hat{\varphi}_1 - ik\frac{Ra^* Pr}{\Omega}\hat{\theta}_1 \\ + \left(\mathcal{D}^2 - k^2\right)\hat{\theta}_1 + 2\Theta_1'(x)\mathcal{D}\hat{\theta}_1, \qquad (43)$$

$$\sigma\left(\mathcal{D}^2 - k^2\right)\hat{\varphi}_2 = -ikRa^* Pr\,\hat{\theta}_2 \\ + Pr\left(\mathcal{D}^4 - 2k^2\mathcal{D}^2 + k^4\right)\hat{\varphi}_2 + \frac{L_\perp^2 \Omega}{L_\parallel}\hat{\varphi}_2, \qquad (44)$$

$$\sigma\hat{\theta}_2 = ik\left(\Theta_2'(x) + \zeta\right)\hat{\varphi}_2 - ik\frac{Ra^* Pr}{\Omega}\hat{\theta}_2 + \left(\mathcal{D}^2 - k^2\right)\hat{\theta}_2 \\ + 2\Theta_2'(x)\mathcal{D}\hat{\theta}_2 - \frac{1}{N_2(x)}\frac{\Omega}{L_\parallel}\hat{\theta}_2 + \frac{L_\perp^2}{L_\parallel}\hat{\varphi}_2. \qquad (45)$$

Boundary and separatrix conditions (37)–(39) become

$$\varphi_1 = \mathcal{D}^2\varphi_1 = \theta_1 = 0 \quad \text{at} \quad x = -1, \qquad (46)$$
$$\mathcal{D}\varphi_2 = \left(\mathcal{D}^2 - k^2\right)\varphi_2 = \mathcal{D}\theta_2 = 0 \quad \text{at} \quad x = \delta, \qquad (47)$$
$$\varphi_1 = \varphi_2, \quad \mathcal{D}\varphi_1 = \mathcal{D}\varphi_2,$$
$$\left(\mathcal{D}^2\varphi_1 + k^2\varphi_1\right) = \left(\mathcal{D}^2\varphi_2 + k^2\varphi_2\right),$$
$$\left(\mathcal{D}^3\varphi_1 - 3k^2\mathcal{D}\varphi_1\right) = \left(\mathcal{D}^3\varphi_2 - 3k^2\mathcal{D}\varphi_2\right),$$
$$\theta_1 = \theta_2, \quad \mathcal{D}\theta_1 = \mathcal{D}\theta_2 \quad \text{at} \quad x = 0. \qquad (48)$$

Equations (42)–(45), subject to boundary and separatrix conditions (46)–(48), constitute an eigenvalue boundary value problem. We solve the eigenvalue problem numerically using the shooting method[27]; we shoot from the boundaries with matching imposed at $x = 0$. We are interested in the onset of instability: thus for each wavenumber k, we seek the density difference Δn for which $Re(\sigma) = 0$. Having done this, we then identify the minimal, critical, density difference Δn_c, and the accompanying critical wavenumber at which this minimum is attained.

Before proceeding with the analysis of results, it is helpful to utilize the analogy with the thermal convection problem[18] in order to gain insight about a necessary condition for the onset of instability in the plasma problem. The linear two-dimensional convection equations for the fluid streamfunction ψ and temperature perturbation θ are

$$\frac{\partial \nabla^2 \psi}{\partial t} = -Ra^* Pr \frac{\partial \theta}{\partial y} + Pr\nabla^2\nabla^2\psi, \qquad (49)$$

$$\frac{\partial \theta}{\partial t} = \frac{dT}{dz}\frac{\partial \psi}{\partial y} + \nabla^2\theta. \qquad (50)$$

A necessary condition for instability in convection is $\frac{dT}{dz} < 0$ — i.e. an unstable temperature stratification.

In the classical convection problem, $\frac{\mathrm{d}T}{\mathrm{d}z}$ is negative and uniform. Motion is driven by a combined effect of the buoyancy drive term and the advection of the basic state temperature gradient (respectively the first terms on the right hand side in (49) and (50)). In the absence of a temperature gradient, or when the temperature increases with height (stable stratification), convective motions will not ensue. Invoking the analogy between the plasma problem and thermal convection, and thus comparing (50) with (34) and (36), we recognize that $(\Theta' + \zeta)$ is an analogue of $\frac{\mathrm{d}T}{\mathrm{d}z}$. Therefore, a necessary condition for instability is that $(\Theta' + \zeta)$ is negative somewhere. As we shall see in the following section, the nature of the basic state density distribution is such that $(\Theta' + \zeta)$ changes sign within the domain. Thus the domain of the plasma problem contains regions of unstable stratification adjacent to regions of stable stratification.

IV. ONSET OF INSTABILITY

A. The case of equal region widths ($\delta = 1$)

We begin with the case where the core region and the SOL are taken to be of equal width, i.e. $\delta = 1$, and consider first the effect of varying the ion viscosity μ. Figure 3 shows the variation of the critical density difference Δn_c and the critical wavenumber k_c with respect to μ at fixed values of D_n. In the governing equations, (30) and (31), the relevant parameters are Pr and Ra^*Pr; as can be seen from (21), changing μ changes Pr, while keeping the combination Ra^*Pr unchanged. Thus, on reducing μ, the coefficient of the viscosity term in the vorticity equation decreases. This lessens the stabilizing influence of viscosity and is consistent with the universal trend observed in Fig. 3a: on reducing the ion viscosity, the critical density difference required for the onset of instability decreases.

Variation of the critical wavenumber (shown in Fig. 3b) is less straightforward. Two features are apparent: the first is the increase in critical poloidal wavenumber k_c as μ is decreased from $O(1)$ values; the second is the non-monotonic behavior of k_c in the case of $D_n = 10^{-3}$. We focus first on the universal trend, i.e. the initial increase with k_c as μ is decreased, postponing the discussion of the departure from this trend until the end of the section. The shift of the preferred poloidal mode toward smaller cells can be understood with reference to the structure of the solution at the onset of instability. Figure 4 shows contour plots of the critical modes of potential φ, vorticity ω, and log-density θ perturbations, at fixed $D_n = 0.1$ and decreasing values of μ; for each case, the values of Δn_c and k_c follow from Fig. 3. Note that the solutions are periodic in the y direction with wavelength $2\pi/k_c$. For comparison of cell structures in the related Figs. 4, 6, 11, 12, we have chosen to illustrate a portion of the domain of length 2π in the y direction, which encompasses more than one wavelength (but is not periodic). Also

plotted are the underlying basic state log-density gradient Θ' profiles for each case, in which the convectively unstable region is highlighted. When $\mu = 1$, the perturbations take the form of large cells whose wavelength is comparable to the width of the convectively unstable region. This can be seen in Fig. 4a: contours of the potential perturbation φ, and thus the fluid motion, are confined to within the range of the convectively unstable region. Note, however, that the density perturbation extends slightly into the quiescent region owing to diffusion. Decreasing μ leads to a decrease in Δn_c, which, broadly speaking, shifts the basic state gradient Θ' upwards, thus narrowing the extent of the convectively unstable region (compare the bottom row of Fig. 4). This, in turn, reduces both the radial and poloidal scales of the cells; this narrowing of the cells is reflected in the increase of the critical wavenumber. When μ is decreased below some critical value, a second stable region appears and the convectively unstable region becomes localized near the separatrix, sandwiched by convectively stable regions (Fig. 4c). This drastic narrowing of the unstable region is accompanied by a pronounced increase in k_c, which reflects a change to smaller cells localized near the separatrix.

The variation of Δn_c and k_c with respect to D_n, at fixed values of μ, is shown in Fig. 5. While μ directly affects only one of the coefficients in the governing equations, the explicit dependence on D_n is more widespread. In particular, variation of D_n affects the coefficients of all the terms on the right hand side of the vorticity equation ((33), (35)), of which the interchange term is destabilizing, and the viscous and damping terms are stabilizing. Furthermore, D_n comes into the coefficients of two terms in the density equation: the diamagnetic flow term $(Ra^*Pr/\Omega)\partial_y\theta$ and the parallel dissipation term $(\Omega/L_{\parallel})\theta$, both of which are stabilizing. As D_n is varied, the coefficients of all of the stabilizing terms vary as $\sim D_n^{-1}$, while the coefficient of the destabilizing interchange term varies like $\sim D_n^{-2}$. Thus as D_n is decreased from unity, the coefficient of the interchange term increases substantially faster than the coefficients of the stabilizing terms, and hence the critical density difference required for the onset of instability decreases, as seen in Fig. 5a.

The variation of k_c with respect to D_n, shown in Fig. 5b, follows a similar pattern to that with respect to μ (Fig. 3b); note, however, that varying D_n also changes the shape of the basic state gradient. In particular, as D_n is reduced, the transition between Θ'_1 and Θ'_2 becomes sharper. This additional factor plays a role in affecting the structure of the critical modes. This is most clearly visible in contours of θ in Fig. 6. When $D_n = 1$ the unstable region covers all of the core region as well as the majority of the SOL, and θ perturbations penetrate the entire domain (Fig. 6a). As seen in Fig. 6b, on reducing D_n, the width of the unstable region narrows, and with it the extent of θ perturbation, which now penetrates only slightly the convectively stable SOL. As we decrease D_n further (Fig. 6c), a second stable region appears, and θ
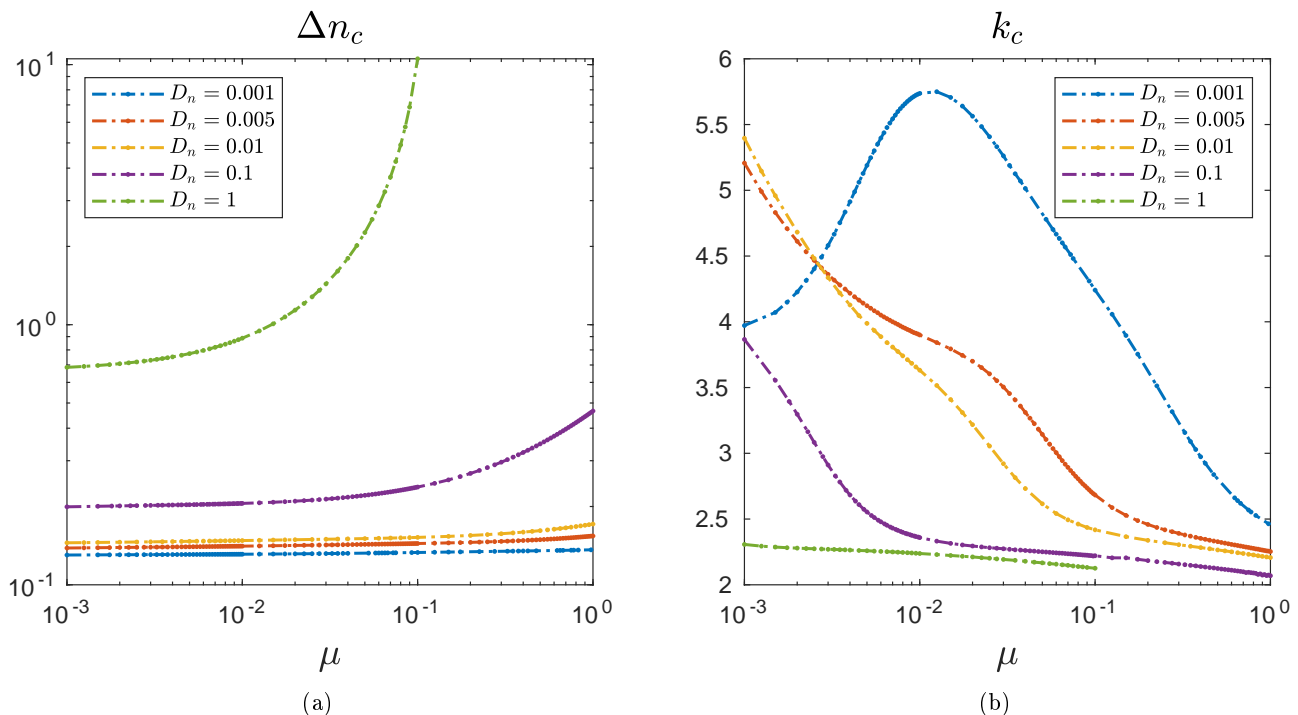
FIG. 3: Variation of (a) the critical density difference Δn_c, and (b) the corresponding critical wavenumber k_c at the onset of instability with respect to the ion viscosity μ, for different values of D_n and $\delta = 1$.

perturbations become localized near the separatrix where the basic state is convectively unstable.

Figure 7 shows the variation of the frequency at the onset of instability. The frequency is negative, which implies propagation of convective cells in the positive y direction. Generally, the magnitude of the frequency increases as D_n is decreased (at a fixed μ). This is consistent with our expectations from our analysis of the single region plasma problem[18], where we found that the frequency at the onset of instability varies roughly like $\gamma \sim -\mu D_n^{-2}$. Following this we would expect the magnitude of the frequency to decrease as μ is decreased. This indeed seems to be the overall trend, although for small D_n (e.g. $D_n = 0.001$ in Fig. 7b) this decrease is not monotonic.

Thus far, we have explained the increase in wavenumber as the diffusion coefficients are decreased. It now remains to address the departure from this trend in cases when μ and D_n are decreased below a certain value (see curves $D_n = 10^{-3}$ and $\mu = 10^{-3}$ in Figs. 3b, 5b respectively). Intuitively, one can expect that this transition is a result of changes in the dominant balance of terms in the governing equations. To explore this issue, we calculate the root mean square (r.m.s.) value of a quantity f_j as

$$f_j^{\mathrm{rms}} = \|f_j\| = \left(\int_{\mathcal{X}_j} f_j \cdot \bar{f}_j \, \mathrm{d}x \right)^{1/2}, \qquad (51)$$

where overbar denotes the complex conjugate, the index

$j = 1, 2$ indicates core and SOL regions respectively, and the corresponding regions of integration are $\mathcal{X}_1 = [-1, 0]$, and $\mathcal{X}_2 = [0, \delta]$. Furthermore, we normalize all calculated r.m.s. values by φ_1^{rms}. This then leads to a convenient graphical representation for the magnitudes of all of the terms in $(33) - (36)$ in terms of bar charts.

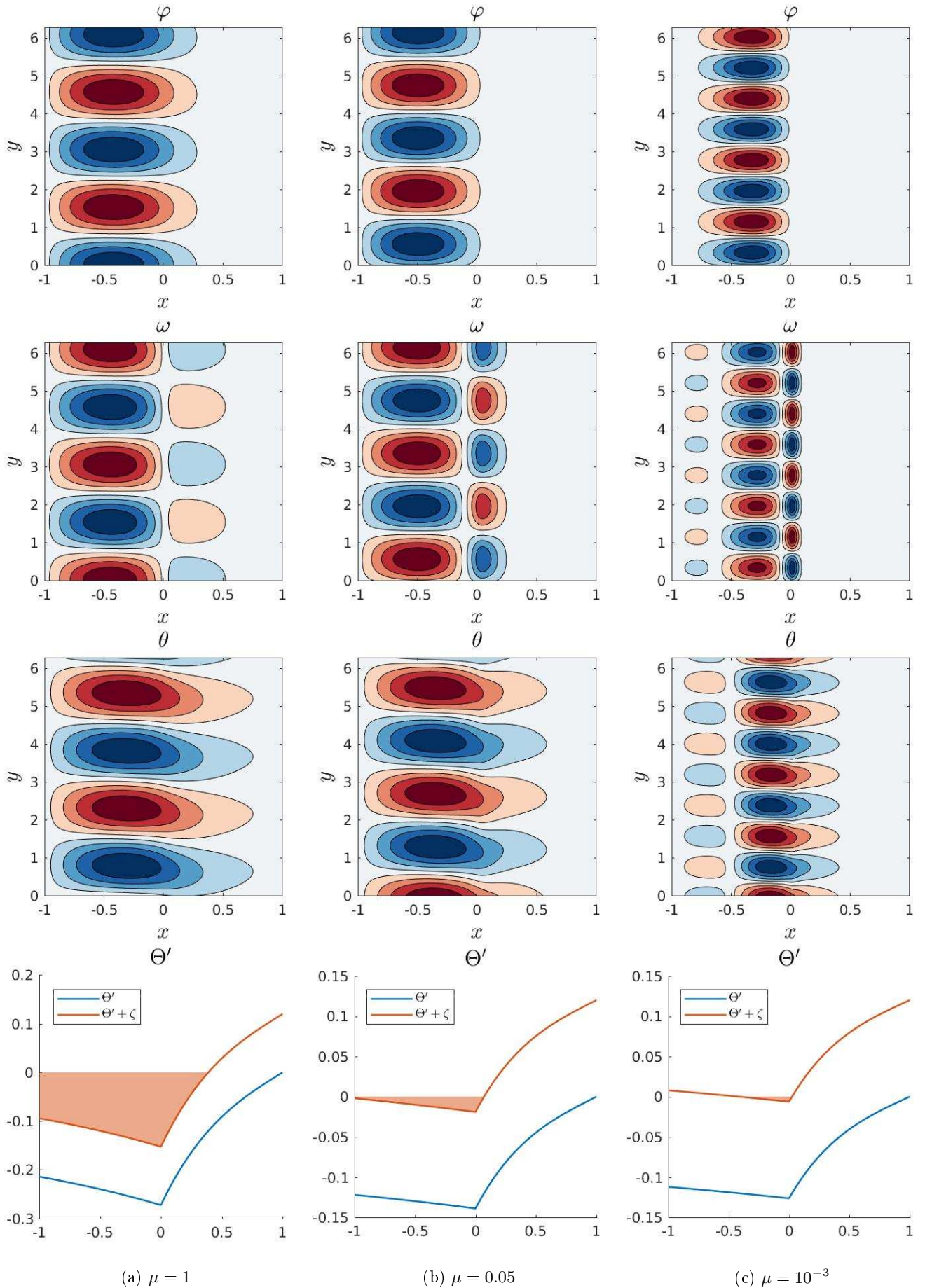(a) $\mu = 1$ (b) $\mu = 0.05$ (c) $\mu = 10^{-3}$

FIG. 4: From top to bottom: contours of potential φ, vorticity ω, log-density θ perturbations, and the underlying basic state log-density gradient Θ' profiles with the convectively unstable region highlighted. Particle diffusivity is fixed at $D_n = 0.1$, ion viscosity μ decreases from left to right: (a) $\mu = 1$, (b) $\mu = 0.05$, (c) $\mu = 10^{-3}$.
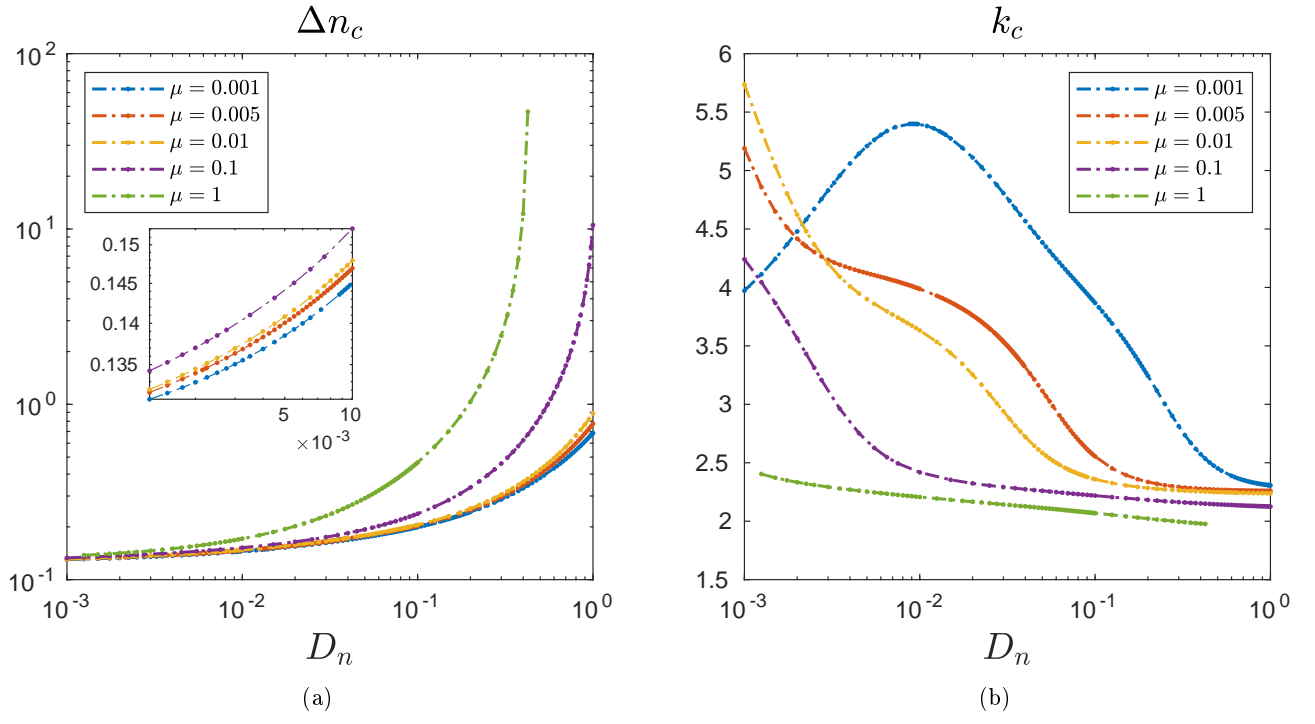
FIG. 5: Variation of (a) the critical density difference Δn_c, and (b) the corresponding critical wavenumber k_c at the onset of instability with respect to the particle diffusivity D_n, for different values of μ and $\delta = 1$.
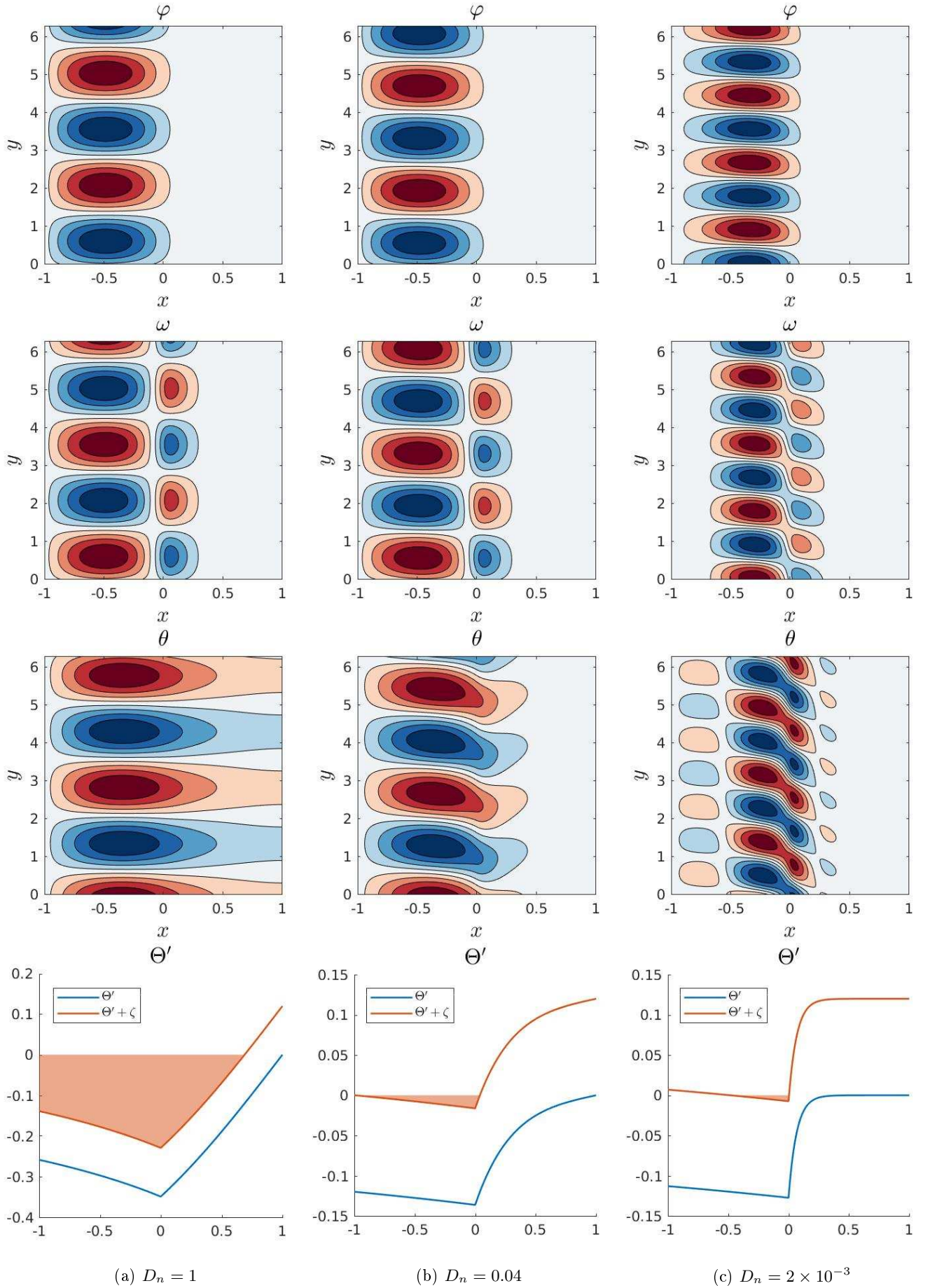
(a) $D_n = 1$ (b) $D_n = 0.04$ (c) $D_n = 2 \times 10^{-3}$

FIG. 6: From top to bottom: contours of potential φ, vorticity ω, log-density θ perturbations, and the underlying basic state log-density gradient Θ' profiles with the convectively unstable region highlighted. Ion viscosity is fixed at $\mu = 0.1$, particle diffusivity D_n decreases from left to right: (a) $D_n = 1$, (b) $D_n = 0.04$, (c) $D_n = 10^{-3}$.
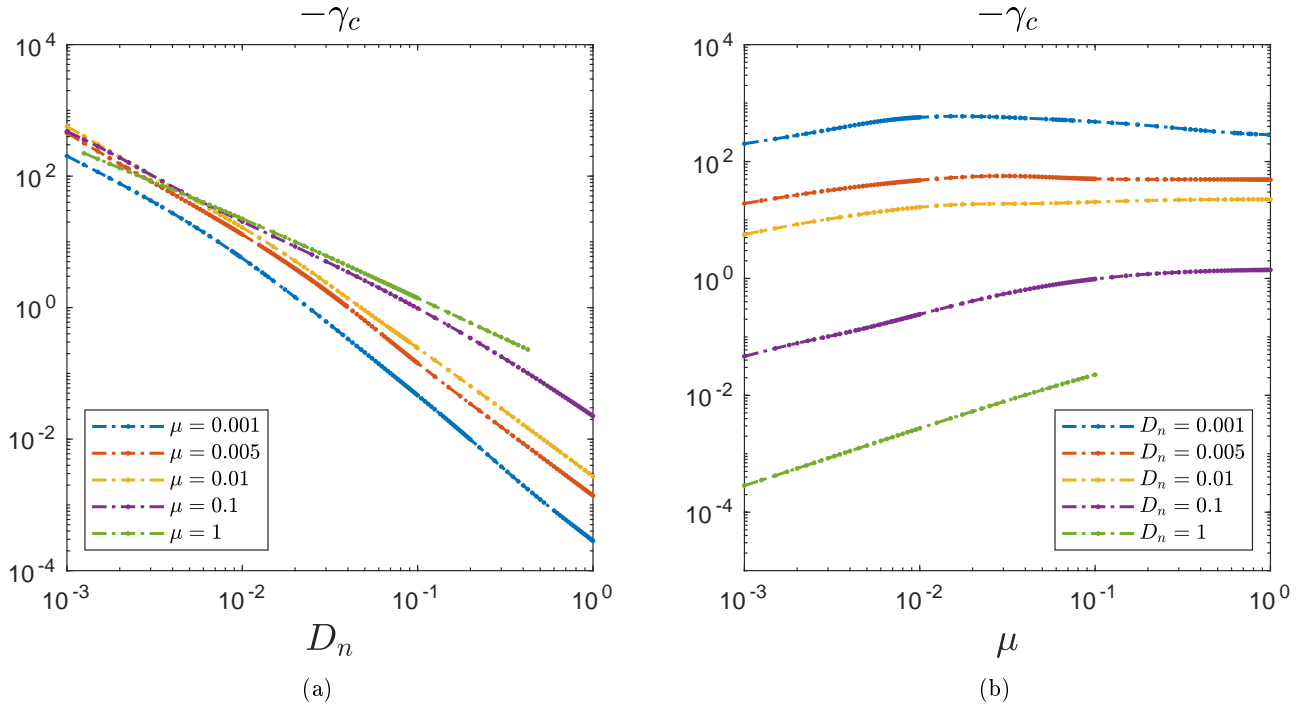
FIG. 7: Variation of the frequency of oscillation associated with the critical mode with respect to (a) the particle diffusivity D_n, and (b) ion viscosity μ.

Figure 8 shows the r.m.s. values of all terms in (33) − (36) for $\mu = 10^{-3}$ and decreasing values of D_n. In the SOL region, the diffusion and parallel loss terms dominate in both the vorticity and density equations in all three cases plotted. On the other hand, in the core, on decreasing D_n there is a marked change in the dominant balance. In particular, on going from $D_n = 10^{-1}$ (Fig. 8a) to $D_n = 10^{-3}$ (Fig. 8c) there is a shift from a state where there is a clear balance between just two terms in each equation to a state where all terms (or all but one in the density equation) become comparable in magnitude. While a first principles explanation of this behavior is elusive, we can gain some understanding by identifying definite trends in the nature of the numerical solution. We can also develop some intuition about the system by exploiting the analogy with thermal convection. In the convection problem, described by eqns. (49), (50), time derivatives vanish at onset and there is a simple relation between the streamfunction and the temperature perturbation: $\psi \sim Ra^* \theta$. Given the oscillatory nature of the instability in the plasma problem, as well as the presence of the non-constant coefficients and a number of other modifications, the relation between the magnitudes of φ and θ will conceivably be more complicated. Nevertheless, the analogy between the two problems provides us with a crude, yet informative, rule of thumb: since $1/Ra^* \sim D_n \mu$ we can expect the ratio $\|\theta\|/\|\varphi\|$ to decrease as D_n and μ are decreased. Indeed, this has been verified in numerical solutions.

In the case with $D_n = 10^{-1}$, shown in Fig. 8a, the balance in the vorticity equation in the core region is between the interchange term and the diffusion term. On reducing D_n, the r.m.s. values of all three terms in the vorticity equation increase. Crucially, on going from $D_n = 10^{-1}$ to $D_n = 10^{-3}$, the time derivative term grows to become comparable in magnitude with the interchange and diffusion terms. This effect can be attributed to the increase in the magnitude of the frequency at onset (see Fig. 7a). The coefficients of the interchange term, $Ra^* Pr \sim D_n^{-2}$, and of the diffusion term, $Pr \sim D_n^{-1}$, also increase as D_n is decreased. We note that although the magnitude of θ itself decreases, the interchange coefficient grows more rapidly — in particular, on varying D_n between 1 and 10^{-3}, $\|\theta\|/\|\varphi\|$ decreases only by a factor of 10. It is thus understandable that the r.m.s. values of the interchange and diffusion terms in the vorticity equation should also increase on decreasing D_n.

The change in the nature of dominant balance in the density equation in the core region can be explained using the arguments laid out above. In the case with $D_n = 10^{-1}$, the balance is between the term describing advection of the basic state density distribution and the diffusion term. Decreasing D_n increases the frequency at onset as well as the coefficient $Ra^* Pr/\Omega \sim D_n^{-1}$, with both of these quantities increasing faster than θ diminishes. Thus, the term representing advection of density by the diamagnetic flow $(Ra^* Pr/\Omega)\partial_y\theta$ grows together with the time derivative term until ultimately all terms,

apart from $-2\Theta'\partial_x\theta$ (which remains sub-dominant for all parameters studied here), are of comparable magnitude.

We note that this change in the nature of the dominant balance in the equations governing the core region coincides with the turning point in the critical k curve. The behavior of k_c as D_n is decreased changes when sub-dominant terms grow sufficiently large to affect the dominant balance.

The variation of the r.m.s. values of all terms in (33) − (36) for $D_n = 10^{-3}$ and decreasing values of μ is shown in Fig. 9. Note that the case with $D_n = \mu = 10^{-3}$ is common to Figs. 9c and 8c. Unlike in the cases presented in Fig. 8, where a clear balance in the SOL between diffusion and parallel loss terms persisted for all values of D_n, here the SOL balance is spread out across all terms with the exception of the time derivative term in the vorticity equation and the $-2\Theta'\partial_x\theta$ term in the density equation. In terms of the balance in the core region, broadly speaking, the pattern depicted in Fig. 9 is similar to that in Fig. 8: on reducing the value of the diffusion coefficient, there is a shift from a state where there is a clear balance between a few terms to a state where all (or nearly all) terms become comparable in magnitude. Starting with $\mu = 10^{-1}$ (Fig. 9a), the dominant terms in the vorticity equation are the interchange and diffusion. In the density equation, with $D_n = 10^{-3}$, the frequency γ and the factor $Ra^* Pr/\Omega$ are large, and thus the dominant balance is between $\partial_t\theta$ and $(Ra^* Pr/\Omega)\partial_y\theta$. On decreasing μ, the r.m.s. values of the dominant terms in both the vorticity and density equations decrease until they become comparable with those of the formerly sub-dominant terms. The reduction in the r.m.s. values of the interchange term $Ra^* Pr \partial_y\theta$ in the vorticity equation, as well as $\partial_t\theta$ and $(Ra^* Pr/\Omega)\partial_y\theta$ in the density equation, can be attributed to the diminishing magnitude of θ. At the same time, the magnitude of the diffusion term in the vorticity equation decreases on account of diminishing Pr.

B. The case of unequal region widths ($\delta \neq 1$)

We now consider the case where the two regions are of different width. Figure 10 shows the variation with respect to δ of the critical density difference Δn_c, critical wavenumber k_c, and frequency γ_c at the onset of instability for a few select (D_n, μ) parameter cases. Evidently, Δn_c is decreasing with δ (Fig. 10a). Furthermore, as δ is decreased toward 0, we expect Δn_c to increase without limit. From equation (27), we see that as $\delta \to 0$, $A_1 \to 0$, and the basic state density tends to a uniform distribution $N_1 \to 1 + \Delta n$. In the absence of an adverse basic state density gradient, the necessary condition for instability cannot be satisfied, and the system is linearly stable for arbitrarily large Δn. The frequency γ_c of the critical mode increases (i.e. becomes less negative) as δ is decreased. In particular, note that in the case with $D_n = 0.1$, $\mu = 0.01$ the frequency changes sign, from negative to positive, as δ is decreased. This implies a
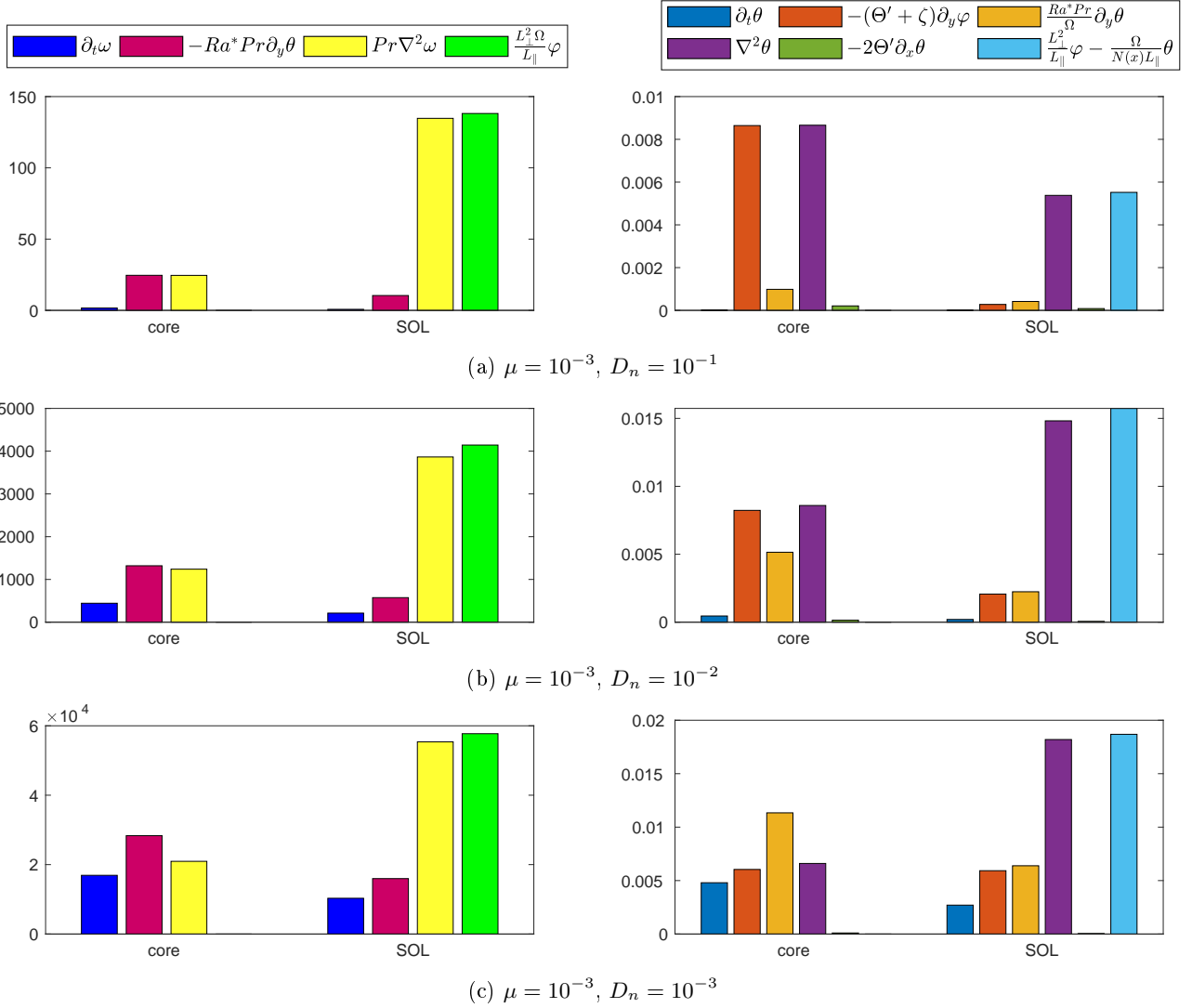
FIG. 8: Root mean square values of individual terms in (33)–(36), normalized with respect to $\|\phi_1\|$, for fixed $\mu = 10^{-3}$ and decreasing values of D_n: (a) $D_n = 10^{-1}$, (b) $D_n = 10^{-2}$, (c) $D_n = 10^{-3}$. Panels on the left show magnitudes of the terms in the vorticity equation in the core and SOL regions, equations (33) and (35), respectively. Similarly, the panels on the right show magnitudes of the terms in the density equation in the core and SOL regions, equations (34) and (36), respectively.

reversal in the direction of propagation of perturbations. It also implies that there exists (at least for this case) a value of δ where the instability is non-oscillatory i.e. $\gamma = 0$.

As δ is decreased from unity, we also observe a tendency of the instability to favor perturbations with larger wavelength, as evidenced by decreasing critical wavenumber for sufficiently small δ (Fig. 10b). In two of the cases ($D_n = 0.1$, $\mu = 0.01$ and $D_n = 1$, $\mu = 0.01$) this decrease in the critical wavenumber is monotonic, whereas in the other ($D_n = 0.01$, $\mu = 0.1$) it is preceded by a small increase in k_c. In the two former cases, this change in the preferred length scale could be attributed to the narrowing of the convectively unstable region. Figure 11 shows

contour plots of potential φ, vorticity ω, and log-density θ perturbations, along with the underlying basic state log-density gradient Θ' profiles, for $D_n = 1$, $\mu = 0.01$ and decreasing values of δ. As seen in the bottom two rows of Fig. 11, as δ is decreased, the extent of the convectively unstable region grows in proportion to the total width of the domain, thus favoring perturbations with larger wavelength.

Contour plots of the critical mode for the case that exhibits non-monotonic variation of k_c with respect to δ are shown in Fig. 12. Clearly, the structure of the solutions in this case is markedly different to that described immediately above. For a start, the underlying basic state density is such that the convectively unstable region is
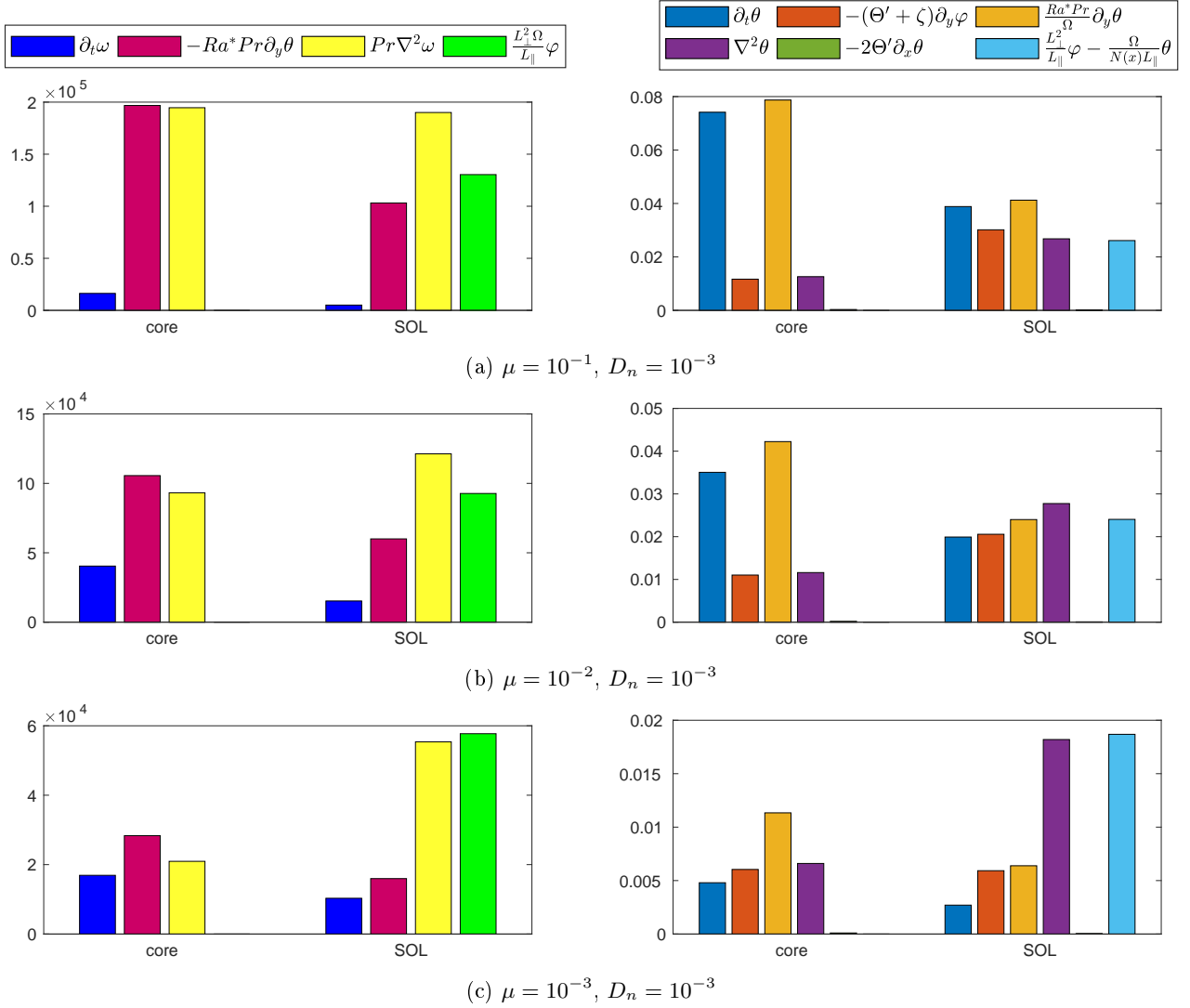
(a) $\mu = 10^{-1}$, $D_n = 10^{-3}$

(b) $\mu = 10^{-2}$, $D_n = 10^{-3}$

(c) $\mu = 10^{-3}$, $D_n = 10^{-3}$

FIG. 9: Root mean square values of individual terms in (33)–(36) for fixed $D_n = 10^{-3}$ and decreasing values of μ: (a) $\mu = 10^{-1}$, (b) $\mu = 10^{-2}$, (c) $\mu = 10^{-3}$.

localized near the separatrix, sandwiched between two stable regions (see bottom row of Fig. 12). For $\delta = 0.6$ (before the peak in Fig. 10b), the fluid motion is confined to the core region and the density perturbations are localized near the separatrix, as seen in the contours of φ and θ in Fig. 12a. Recall from Fig. 10b that as δ is decreased, the critical wavenumber increases initially to a maximum, beyond which further decrease in δ leads to an abrupt decrease in k_c. Contour plots of the critical modes near the maximum of k_c ($\delta = 0.15$) and beyond ($\delta = 0.12$) are shown in Fig. 12b and 12c respectively. There, we observe that the fluid motion is no longer confined to the core region, but instead extends over the whole width of the domain. Moreover, the critical mode is now characterized by non-zero flow velocities on the $x = \delta$ boundary. The peak of the density perturbation is no longer in the region where the basic state is con-

vectively unstable, but instead is localized to the thin SOL.

Finally, we observe that as δ is increased, the critical density difference, the critical wavenumber and the frequency quickly tend toward asymptotic values associated with the limit of $\delta \to \infty$. In this limit the problem reduces to something akin to convection in a layer of fluid bounded from one side by an infinite expanse of stably stratified fluid.

V. DISCUSSION

In this paper we have performed a comprehensive linear stability analysis of a simple core-SOL model of interchange motions in the plasma edge of magnetic confinement devices. We have investigated how the stability
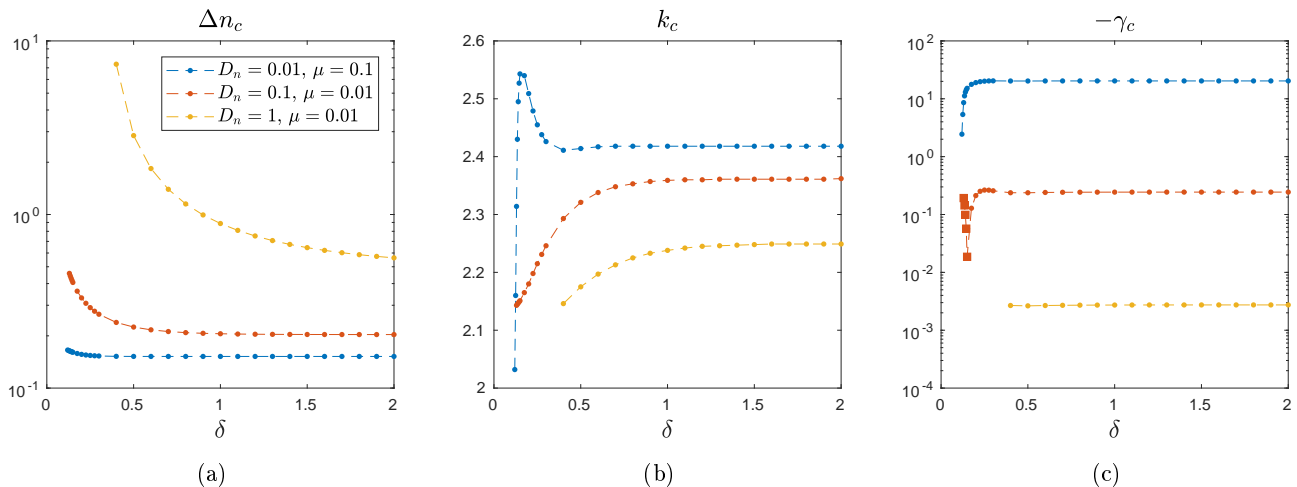
FIG. 10: Variation of (a) the critical density difference, (b) the corresponding critical wavenumber, and (c) the frequency at the onset of instability with respect to the width ratio δ. In (c), square markers indicate positive frequency, i.e. $-\gamma < 0$.

threshold and the structure of the critical mode change as functions of particle diffusivity, ion viscosity, and the ratio of the widths of the two regions.

We find that decreasing the values of the diffusion parameters lowers the critical density difference at the onset of instability, thus leading to a more unstable system. Furthermore, we identify two distinct regimes at onset: one where the critical modes span the entire region of the core in the model, and even extend into the scrape-off layer; and the other where the critical modes are localized in a thin region at the separatrix. The emergence of these two regimes is linked to the nature of the underlying basic state density gradient (see Figs. 4, 6). In the first — which occurs when neither the (normalized) ion viscosity nor particle diffusivity are particularly small — the form of the basic state gradient results in the domain being divided into a convectively unstable region and a convectively stable region. The perturbations take the form of cells whose radial extent and poloidal wavelength are comparable to the width of the unstable region. In the second regime, the basic state gradient splits the domain into three parts: a convectively unstable region in the vicinity of the separatrix, sandwiched by convectively stable regions. The additional stable region appears when either the ion viscosity or the particle diffusivity are decreased below some critical values. The resulting drastic narrowing in the extent of the convectively unstable region leads to an increase in the critical wavenumber, indicating a change to smaller cells localized near the separatrix.

As the width ratio of the two regions δ is increased from unity, the stability threshold quickly becomes independent of δ (see Fig. 10). On the other hand, decreasing δ from unity significantly affects both the onset of instability and the structure of the most unstable mode (see Fig. 12). Specifically, as δ is decreased, the system be-

comes increasingly more stable. This is expected, since in the limit of $\delta \to 0$ the basic state density gradient vanishes, and thus the necessary condition for instability cannot be satisfied. It is, however, worth noting that our model inherently relies on the presence of both core and SOL regions, and hence the limit of $\delta \to 0$ should not be thought of as a core-only model.

The analysis included in this paper opens up a number of avenues for further investigation, both in terms of the linear stability problem and also the nonlinear development of the instability. The model under consideration here contains a number of simplifying assumptions. Retaining the 2D slab geometry, it would be of interest to understand how the onset of linear instability is affected by the relaxation of the Boussinesq approximation and the assumptions of isothermal electrons and cold ions. Our detailed investigation of the nature of the onset of instability paves the way for a systematic exploration of the nonlinear evolution. Having nailed down the stability threshold, we are in a position to assess the degree of supercriticality of any nonlinear computation and, indeed, to determine whether subcritical solutions are feasible. In the nonlinear regime, it is of particular interest to study the evolution of the system in order to investigate whether the range of distinct behavior at the onset of instability has consequences for transport in the SOL when the system is driven to a turbulent state. Furthermore, whereas drift wave modes are linearly damped, and hence play no important role in the current study, they may be significant in terms of the nonlinear evolution. As discussed by Scott[28], drift waves, which are subcritical, can sustain finite amplitude turbulence, and hence their dynamics must be considered in concert with the nonlinear evolution of interchange modes.
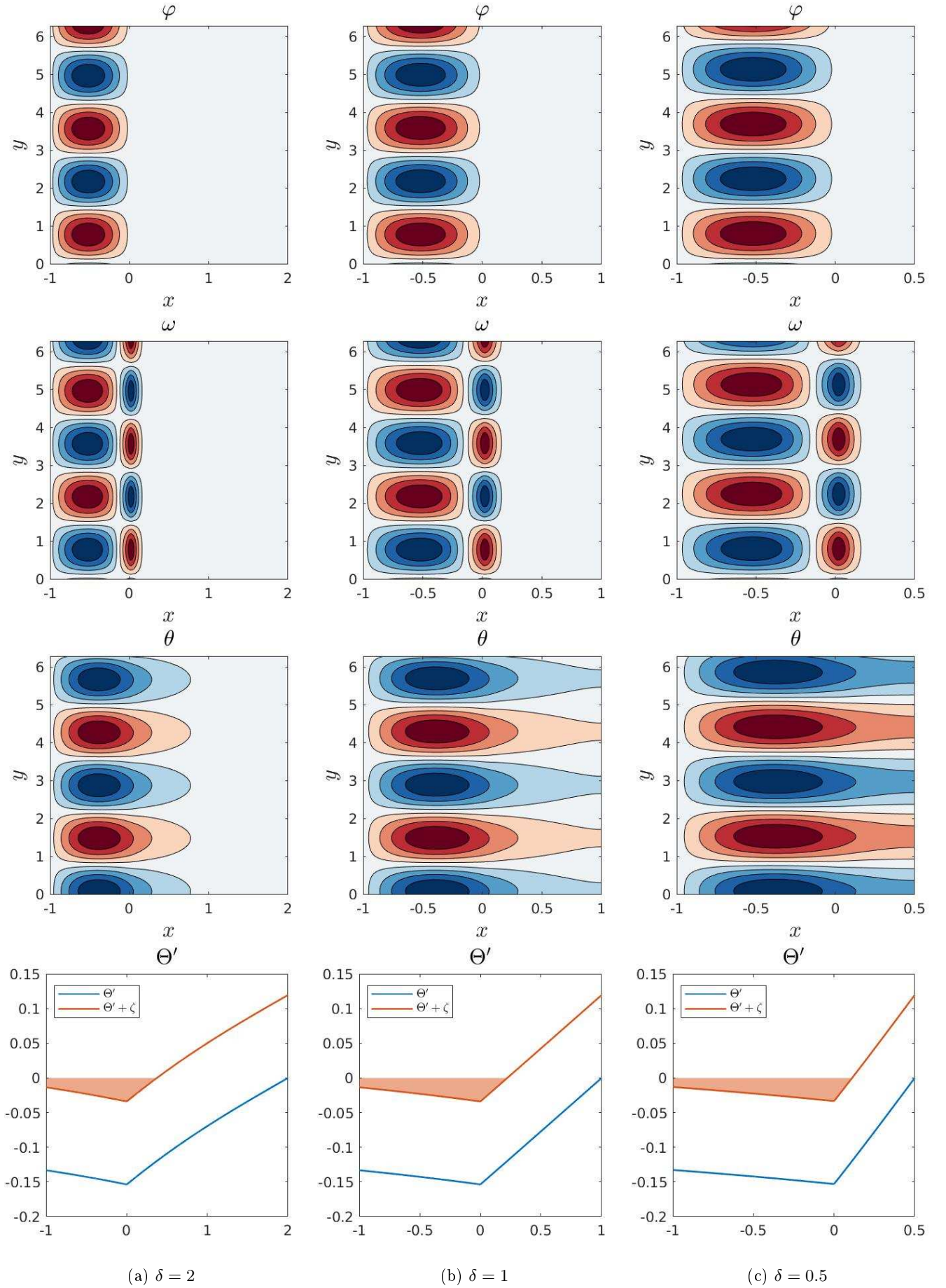
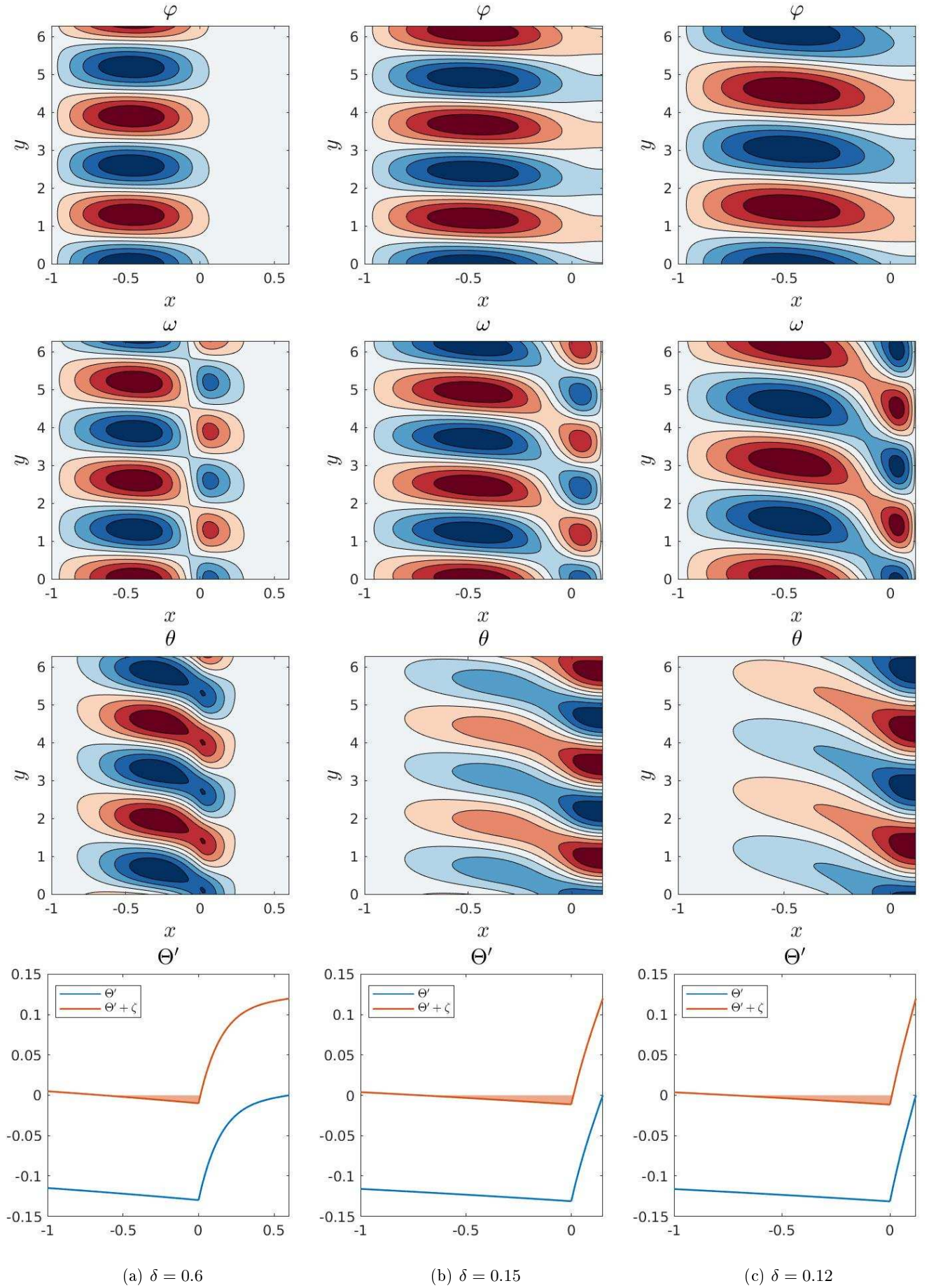(a) $\delta = 2$ (b) $\delta = 1$ (c) $\delta = 0.5$

FIG. 11: From top to bottom: contours of potential φ, vorticity ω, log-density θ perturbations, and the underlying basic state log-density gradient Θ' profiles, with the convectively unstable region highlighted. Ion viscosity and particle diffusivity are fixed at $D_n = 1$, $\mu = 0.01$; width ratio is (a) $\delta = 2$, (b) $\delta = 1$, (c) $\delta = 0.5$.

FIG. 12: From top to bottom: contours of potential φ, vorticity ω, log-density θ perturbations, and the underlying basic state log-density gradient Θ' profiles, with the convectively unstable region highlighted. Ion viscosity and particle diffusivity are fixed at $D_n = 0.01$, $\mu = 0.1$; width ratio is (a) $\delta = 0.6$, (b) $\delta = 0.15$, (c) $\delta = 0.12$.

ACKNOWLEDGMENTS

DATA AVAILABILITY STATEMENT

The data that support the findings of this study are available from the corresponding author upon reasonable request.

[1] S. I. Krasheninnikov, D. A. D'Ippolito, and J. R. Myra, "Recent theoretical progress in understanding coherent structures in edge and SOL turbulence," J. Plasma Phys. **74**, 679 (2008).

[2] D. A. D'Ippolito, J. R. Myra, and S. J. Zweben, "Convective transport by intermittent blob-filaments: comparison of theory and experiment," Phys. Plasmas **18**, 060501 (2011).

[3] W. Fundamenski, *Power Exhaust in Fusion Plasmas* (Cambridge University Press, 2010).

[4] Y. Sarazin and P. Ghendrih, "Intermittent particle transport in two-dimensional edge turbulence," Phys. Plasmas **5**, 4214–4228 (1998).

[5] P. Ghendrih, Y. Sarazin, G. Attuel, S. Benkadda, P. Beyer, G. Falchetto, C. Figarella, X. Garbet, V. Grandgirard, and M. Ottaviani, "Theoretical analysis of the influence of external biasing on long range turbulent transport in the scrape-off layer," Nucl. Fusion **43**, 1013 (2003).

[6] P. Ghendrih, Y. Sarazin, G. Attuel, S. Benkadda, P. Beyer, G. Darmet, G. Falchetto, C. Figarella, X. Garbet, V. Grandgirard, and M. Ottaviani, "Statistical analysis of turbulent front propagation in the scrape-off-layer," J. Nucl. Mater. **337**, 347–351 (2005).

[7] N. Bisai, A. Das, S. Deshpande, R. Jha, P. Kaw, A. Sen, and R. Singh, "Simulation of plasma transport by coherent structures in scrape-off-layer tokamak plasmas," Phys. Plasmas **11**, 4018–4024 (2004).

[8] P. Beyer, Y. Sarazin, X. Garbet, P. Ghendrih, and S. Benkadda, "2d and 3d boundary turbulence studies," Plasma Phys. Controlled Fusion **41**, A757 (1999).

[9] O. E. Garcia, V. Naulin, A. H. Nielsen, and J. J. Rasmussen, "Computations of intermittent transport in scrape-off layer plasmas," Phys. Rev. Lett. **92**, 165003 (2004).

[10] O. E. Garcia, J. Horacek, R. A. Pitts, A. H. Nielsen, W. Fundamenski, J. P. Graves, V. Naulin, and J. J. Rasmussen, "Interchange turbulence in the TCV scrape-off layer," Plasma Phys. Controlled Fusion **48**, L1–L10 (2005).

[11] O. E. Garcia, J. Horacek, R. Pitts, A. H. Nielsen, W. Fundamenski, V. Naulin, and J. J. Rasmussen, "Fluctuations and transport in the TCV scrape-off layer," Nucl. Fusion **47**, 667 (2007).

[12] W. Fundamenski, O. E. Garcia, V. Naulin, R. A. Pitts, A. H. Nielsen, J. J. Rasmussen, J. Horacek, J. P. Graves, and JET EFDA contributors, "Dissipative processes in interchange driven scrape-off layer turbulence," Nucl. Fusion **47**, 417 (2007).

[13] N. Yan, A. H. Nielsen, G. S. Xu, V. Naulin, J. J. Rasmussen, J. Madsen, H. Q. Wang, S. C. Liu, W. Zhang, L. Wang, and B. N. Wan, "Statistical characterization of turbulence in the boundary plasma of east," Plasma Phys. Controlled Fusion **55**, 115007 (2013).

[14] F. Militello, W. Fundamenski, V. Naulin, and A. H. Nielsen, "Simulations of edge and scrape off layer turbulence in Mega Ampere Spherical Tokamak plasmas," Plasma Phys. Controlled Fusion **54**, 095011 (2012).

[15] F. Militello, P. Tamain, W. Fundamenski, A. Kirk, V. Naulin, A. H. Nielsen, and the MAST team, "Experimental and numerical characterization of the turbulence in the scrape-off layer of MAST," Plasma Phys. Controlled Fusion **55**, 025005 (2013).

[16] O. E. Garcia, V. Naulin, A. H. Nielsen, and J. J. Rasmussen, "Turbulence and intermittent transport at the boundary of magnetized plasmas," Phys. Plasmas **12**, 062309 (2005).

[17] O. E. Garcia, V. Naulin, A. H. Nielsen, and J. J. Rasmussen, "Turbulence simulations of blob formation and radial propagation in toroidally magnetized plasmas," Phys. Scr. **T122**, 89–103 (2006).

[18] F. Wilczynski, D. W. Hughes, S. Van Loo, W. Arter, and F. Militello, "Stability of scrape-off layer plasma: A modified Rayleigh–Bénard problem," Phys. Plasmas **26**, 022510 (2019).

[19] F. Wilczynski and D. W. Hughes, "Stability of two-layer miscible convection," Phys. Rev. Fluids **4**, 103502 (2019).

[20] L. Easy, F. Militello, J. Omotani, B. Dudson, E. Havlíčková, P. Tamain, V. Naulin, and A. H. Nielsen, "Three dimensional simulations of plasma filaments in the scrape off layer: A comparison with models of reduced dimensionality," Phys. Plasmas **21**, 122515 (2014).

[21] L. Easy, F. Militello, J. Omotani, N. Walkden, and B. Dudson, "Investigation of the effect of resistivity on scrape off layer filaments using three-dimensional simulations," Phys. Plasmas **23**, 012512 (2016).

[22] J. T. Omotani, F. Militello, L. Easy, and N. R. Walkden, "The effects of shape and amplitude on the velocity of scrape-off layer filaments," Plasma Phys. Controlled Fusion **58**, 014030 (2015).

[23] G. Q. Yu, S. I. Krasheninnikov, and P. N. Guzdar, "Two-dimensional modelling of blob dynamics in tokamak edge plasmas," Phys. Plasmas **13**, 042508 (2006).

[24] R. V. Mendes and J. P. Bizarro, "Analytical study of growth estimates, control of fluctuations, and conservative structures in a two-field model of the scrape-off layer," Phys. Plasmas **24**, 012303 (2017).

[25] J. Madsen, V. Naulin, A. H. Nielsen, and J. J. Rasmussen, "Collisional transport across the magnetic field in drift-fluid models," Phys. Plasmas **23**, 032306 (2016).

[26] R. D. Hazeltine and F. L. Waelbroeck, *The Framework of Plasma Physics* (Westview, 2004).

[27] J. Stoer and R. Bulirsch, *Introduction to Numerical Analysis*, Vol. 12 (Springer Science & Business Media, 2013).

[28] B. D. Scott, "The nonlinear drift wave instability and its role in tokamak edge turbulence," New J. Phys. **4**, 52 (2002).